Corrosion Behavior of Weathering Steel Q450NQR1 and Welded Metal using Flux-Cored Wire in 0.01 mol/L NaHSO₃ Solution

Minghua Zhang[1,2,], Shuai Wu[1], Qianchao Zhang[1], Tangqing Wu[3], Bo Hong[1,2], Yifeng Xiao[1,2], Jinwen Qian[1,2], Fucheng Yin[3]*

[1] Key Laboratory of Welding Robot and Application Technology of Hunan Province, Xiangtan, 411105, China;
[2] School of Mechanical Engineering, Xiangtan University, Xiangtan, 411105, China;
[3] Key Laboratory of Materials Design and Preparation Technology of Hunan Province, Xiangtan University, Xiangtan, 411105, China
[*]E-mail: mhzhang@xtu.edu.cn

In this paper, the corrosion behaviors of weathering steel Q450NQR1 and weld metals of solid and flux-cored wires were studied by microstructure observation, electrochemical techniques and scanning electron microscopy. The results show that the microstructure of weld metal using flux-cored wire is mainly consisted of fine acicular ferrite and granular bainite, with some side plate ferrite and polygonal ferrite. The corrosion rate of the weld metal of flux-cored wire is smaller than those of the base metal and the weld metal of solid wire. Although the three specimens have similar corrosion processes in the solution, the composition, generation and evolution of the corrosion product layer play an important role in the corrosion process. The flux-cored wire is a potential and viable weld wire choice for gas metal arc welding.

1. INTRODUCTION

When steels are exposed to natural atmospheric environment, an electrochemical dissolution reaction takes place on the steel surfaces, which leads to corrosion failure of the steel materials. Atmospheric corrosion is responsible for over 50% of the total corrosion loss of iron and steels [1]. Weathering steel is a low-alloy steel with properties of anti-atmospheric corrosion, to which mainly Cu, P, Cr and Ni are added [2]. A compact and uniform rust layer can be formed on the weathering steel surface when they are used in the atmospheric environment. The rust layer is closely integrated with the

steel substrate and prevents the steel from contacting corrosive media in industrial and marine atmospheres, effectively improving its corrosion resistance [3-7].

Welding is the most important manufacturing technology in the production of steel structures. Selecting efficient welding technology and excellent welding materials is the key to improving the production efficiency and ensuring the performance of welding steel structures. Gas metal arc welding (GMAW) with solid wire is currently the main welding process adopted for weathering steels. As has been reported [8], using solid wire can decrease the cold crack sensitivity of weld metal during welding and gain an approximately equal strength and plasticity as that of the base metal. However, the toughness of the weld metal at -40°C is unsatisfactory. Flux-cored wire arc welding (FCAW) is a high-efficiency semi-automatic and automatic welding process. By reasonably adjusting the components of flux-cored wire, a good weld appearance and excellent mechanical properties such as strength, plasticity and low-temperature toughness can be obtained [9]. However, there is little research on atmospheric corrosion resistance for weld metal of flux-cored wire.

To meet the requirements of producing lightweight vehicles and prolonging their service life, weathering steel Q450NQR1 with a yield strength of 450 MPa and good corrosion resistance has been developed. At present, it is widely used in the production of railway vehicles in China. According to the weldability of weathering steel Q450NQR1, we have developed a specific flux-cored wire [10] and studied its tensile strength, plasticity, low-temperature toughness and fatigue strength [11]. As a systematic study, the corrosion behavior of the weld metal of flux-cored wire in a simulated atmospheric environment was analysed via optical microscopy (OM)，electrochemical methods and scanning electron microscopy (SEM). This study can provide theoretical guidance to develop a new and optimal flux-cored wire for exclusive use of weathering steel Q450NQR1.

2. MATERIAL AND METHODS

2.1 Material

The base metal used in this study was weathering steel Q450NQR1, with its chemical composition shown in Table 1. It was welded by solid wire arc welding and flux-cored wire arc welding respectively. The welding power source was a Panasonic KR-500 machine, and the shielding gas was 100% CO_2. The welding parameters are shown in Table 2. The chemical compositions of the weld metal of solid wire arc welding and flux-cored wire arc welding are listed in Table 1. In this paper, the weld metals of solid wire arc welding and flux-cored wire arc welding were named specimens W1 and W2, respectively. After welding, metallographic specimens were prepared and etched by 4% nitric acid alcohol solution. The microstructure was observed under Zeiss Primotech optical microscope.

Table 1. Chemical compositions of the base metal and weld metals (wt. %)

Materials	C	Mn	Si	S	P	Ni	Cr	Cu	Mo	V	Ti	Al
Base metal	0.053	1.08	0.22	0.006	0.018	0.143	0.52	0.215	0.005	-	-	-
W1	0.06	1.25	0.40	0.007	0.013	0.314	0.47	0.242	0.007	0.001	0.03	0.008
W2	0.03	1.01	0.36	0.003	0.006	0.65	0.50	0.34	0.009	0.01	0.04	0.012

Table 2. Welding parameters used in the paper

Voltage U /V	Current I /A	Welding speed v / mm min^{-1}	Gas-flow rate q/ L min^{-1}	Interlayer temperature T / °C
30	220	380	15 ~ 20	< 100

Through wire-electrode cutting, 10 mm × 10 mm × 3 mm samples of the base metal, specimens W1 and W2 were obtained. After edge grinding, a copper conductor was brazed on the back of the samples. The non-working surfaces of the samples were sealed by epoxy resin. The working surface of the samples were ground by waterproof abrasive SiC paper until 1500# and then polished to a mirror-like finish. After that, the samples were cleaned by deionized water and alcohol and sequentially dried by cold air and stored in a desiccator for use.

2.2 Electrochemical procedure

To simulate an industrial atmospheric environment, a 0.01 mol/L NaHSO$_3$ solution was used in the experiment with the temperature of 45 °C and a period of 15 days. The electrochemical test was operated by using a CS350 electrochemical measurement system. All experiments were performed in a three-electrode electrochemical cell, with a platinum electrode as the counter electrode, a saturated calomel electrode (SCE) as the reference electrode and a testing sample as the working electrode. The specimens were immersed into the solution, and the jar was sealed with silica gel. Three parallel experiments were conducted to ensure the validity of the experimental data.

During the potentiodynamic polarization curve test, the voltage range was from −250 mV to +250 mV (vs. OCP) with a scanning rate of 0.5 mV s^{-1}. The fitting and analysis of the potentiodynamic polarization curve data were conducted via Origin 8.0 software. During the electrochemical impedance spectroscopy (EIS) test, the frequency range was from 100 kHz to 0.01 Hz and the amplitude of the sinusoidal voltage signal was 5 mV. The EIS results were fitted and analysed by ZsimpWin data processing software.
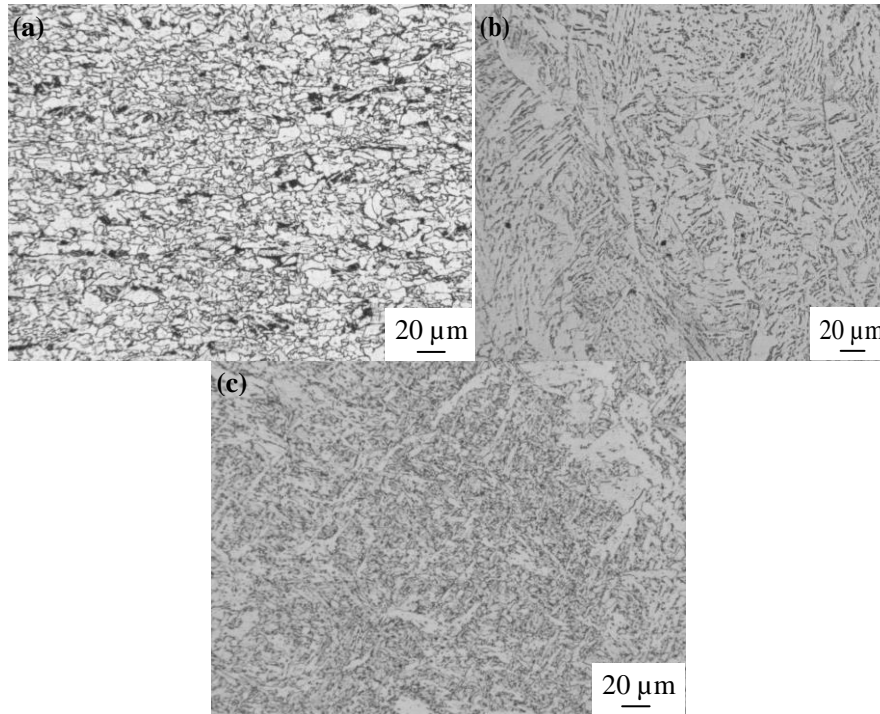
2.3 Corrosion Products Analysis

After the experiment, the specimens were taken from the jar, rinsed with deionized water and ethanol and then dried by cold air. The morphologies of the corrosion products on the surfaces and cross-sections of the samples were observed by scanning electron microscopy (SEM, JSM-6360LV). The components of the corrosion products were analysed by energy dispersive spectroscopy (EDS).

3. RESULTS

3.1 Microstructure observation

As shown in Fig. 1a, the microstructure of the base metal is consisted of ferrite (white) and pearlite (black). The microstructure of specimen W1 is mainly composed of proeutectoid ferrite and side

plate ferrite, where the former precipitats along the austenite grain boundary (Fig. 1b). Some polygonal ferrite and carbonization are also embedded in the microstructure. The average grain size is larger than that of the base metal. As shown in Fig. 1c, fine acicular ferrite and granular bainite are distributed crossly in the weld metal of flux-cored wire arc welding (specimen W2), with some side plate ferrite and polygonal ferrite.

Figure 1. Microstructure of (a) base metal; (b) W1; (c) W2

3.2 Analysis of corrosion products

The morphologies of the corrosion products on the specimen surfaces after 15 days of exposure in the NaHSO$_3$ solution are shown in Fig. 2, with the corresponding EDS analysis results in Table 3. After a 15-day exposure, as shown in Fig. 2a, the corrosion products on the base metal surface are compact and integrated, with some light and loose corrosion products scattered on it. As manifested in the red-oval tile in the magnification of the corrosion product (Fig. 2b), some small cracks can be observed on the corrosion products. The cracks may take place during the dehydration process after the exposure, but it also indicates that the mechanical property of the corrosion product is not good enough. The EDS results show that the light and loose corrosion products are composed of Fe, S and O, thus verifying that Fe oxides and sulfides are the main components of the light layer. However, a small amount of Cr is observed in the compact and integrated corrosion product, indicating that Fe and Cr oxides may be the dominant component.
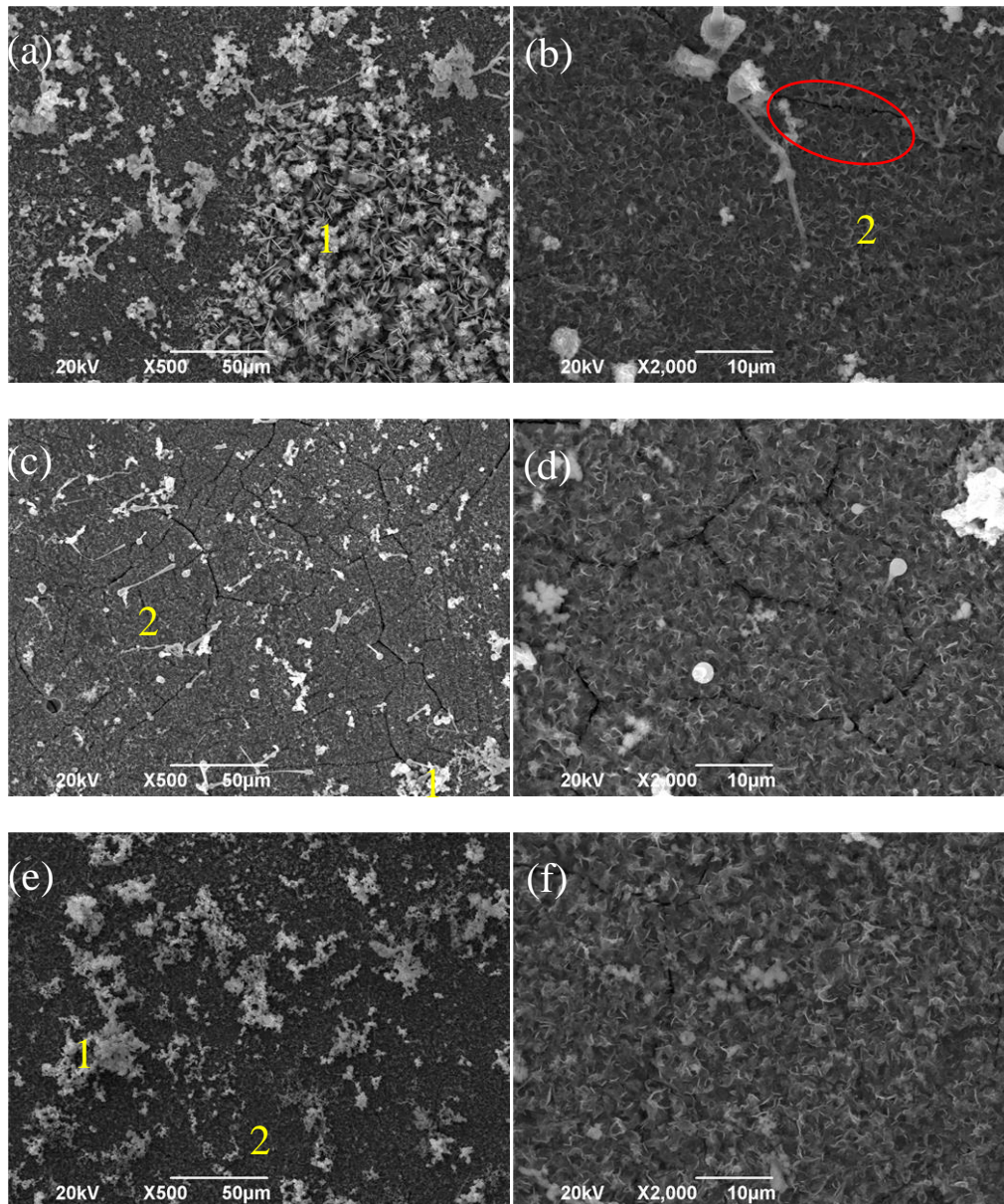
Figure 2. Corrosion product morphologies exposure to the NaHSO₃ solution: base metal (a and b), W1 (c and d) and W2 (e and f)

As shown in Figs. 2c and d, the corrosion products on the weld metal of solid wire arc welding are also compact and integrated, with little light and loose corrosion products distributed on the surface. However, compared with the corrosion products on the base metal, more cracks are observed on the surface, and the average width of the cracks is larger than that on the base metal surface, indicating the poor mechanical property of the corrosion product on specimen W1. The EDS analysis shows that the main components of the corrosion products are similar to those on the base metal surface. The most complete and densest corrosion product films are detected on the surface of the weld metal of flux-cored wire arc welding (Fig. 2e and f), and no cracks are observed on the morphologies of the corrosion products, reflecting the good mechanical properties of the corrosion product. The EDS results show that the main components of the corrosion products are the oxides of Fe and Cr.
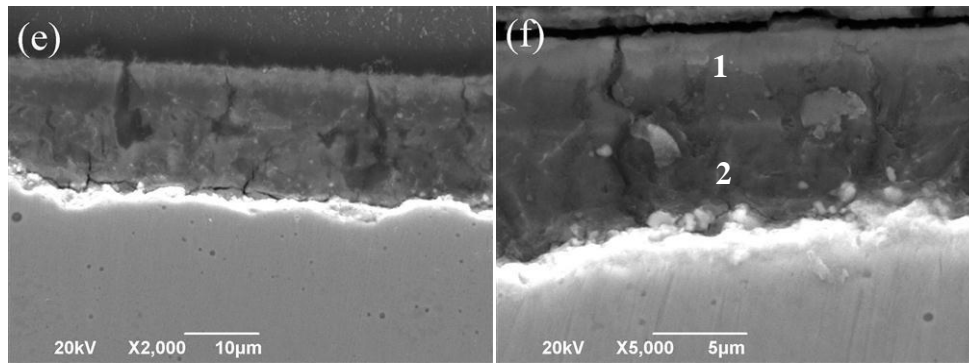
Table 3. Chemical composition of the corrosion surface rust (wt. %)

Materials		O	S	Fe	Cr
Base metal	1	24.54	11.96	63.50	-
	2	11.72	30.13	56.12	2.02
W1	1	21.74	26.79	51.47	-
	2	5.38	32.29	61.06	1.17
W2	1	33.74	14.28	51.98	-
	2	9.07	31.01	58.00	1.92

3.3 Analysis of cross-section

The cross-section morphologies of the base metal, specimens W1 and W2 after 15 days of exposure in the 0.01 mol/L $NaHSO_3$ solution are shown in Fig. 3, with the corresponding EDS analysis results in Table 4. The corrosion product on the base metal is compact and integrated, with a thickness of approximately 8.6 µm. However, obvious cracks can be detected under the corrosion product, which is consistent with the results of the corresponding morphologies of the corrosion products (Figs. 2a and b). The EDS results show that Fe oxides and sulfides are the main components of the outer layer, while more O, Fe and Cr are observed in the inner layer. The corrosion product on the surface of specimen W1 presents the same morphology, with a thickness of approximately 9.2 µm but few cracks on it. The EDS analysis shows that the main components of the corrosion products on the cross-section morphologies are similar to those on the base metal surface, and only a small amount of Ni is found in the inner layer of the corrosion product. For specimen W2, a thick corrosion product layer (approximately 16.5 µm) is shown in Fig. 3e and f. It is compact and integrated, and more Cr and Ni are detected by the EDS analysis.
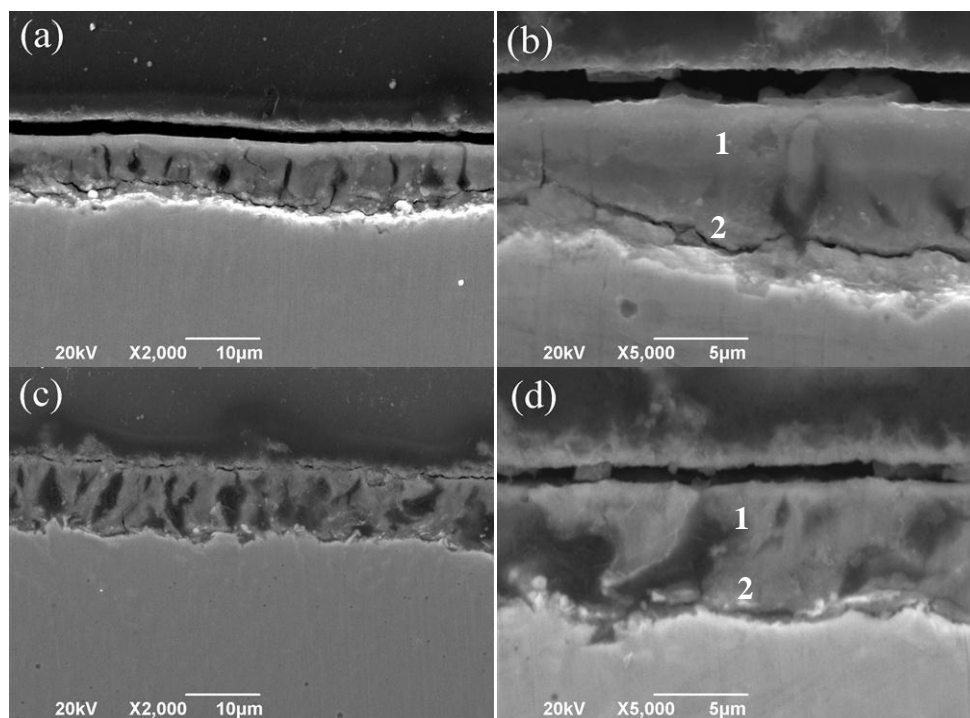
Figure 3. Cross-section morphologies after exposure to the NaHSO₃ solution: base metal (a and b), W1(c and d) and W2 (e and f)

**Table 4.** Chemical composition of the corrosion cross-section rust (wt. %)

Materials		O	S	Cr	Ni	Cu	Fe
Base metal	1	15.24	27.33	2.67	-	-	54.76
	2	20.32	5.21	5.92	-	-	68.55
W1	1	19.44	27.69	2.78	-	-	50.09
	2	26.10	10.56	4.41	3.45	-	55.48
W2	1	16.70	25.29	1.59	2.60	2.86	50.96
	2	20.96	10.23	6.72	12.72	-	49.36

3.4 Analysis of open circuit potential

The evolution of the open circuit potential (OCP) for the base metal, and specimens W1 and W2 in 0.01 mol/L NaHSO₃ solution is shown in Fig. 4. When the specimens are immersed in the solution, their OCPs decrease quickly at the beginning of the experiment and then increase slowly with fluctuations, as shown in Fig. 4a. In the first hour, the OCP of the base metal is the most negative, and the OCP of specimen W2 is the most positive. An hour later, the OCP of specimen W2 is 25 mV more positive than that of the base metal.
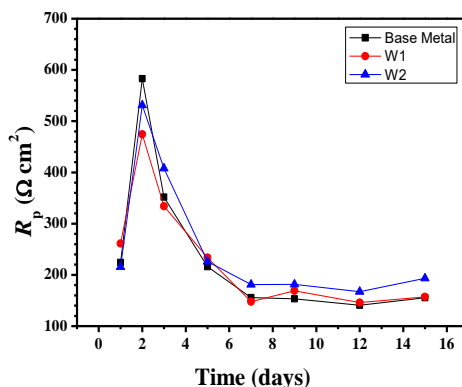
The OCP evolutions for the base metal, and specimens W1 and W2 during an extended period of 15 days are plotted in Fig. 4b. The OCP increases sharply in the first two days and then decreases quickly in the next two days, after which it slowly increases again with some fluctuations. The more positive the OCP is, the higher the corrosion resistance [12]. Therefore, it is reasonable to speculate that the corrosion rate of the specimen is the slowest on the second day. Moreover, the OCP of specimen W2 is highest among the tested specimens after 5 days of exposure, indicating that it has the highest corrosion resistance.
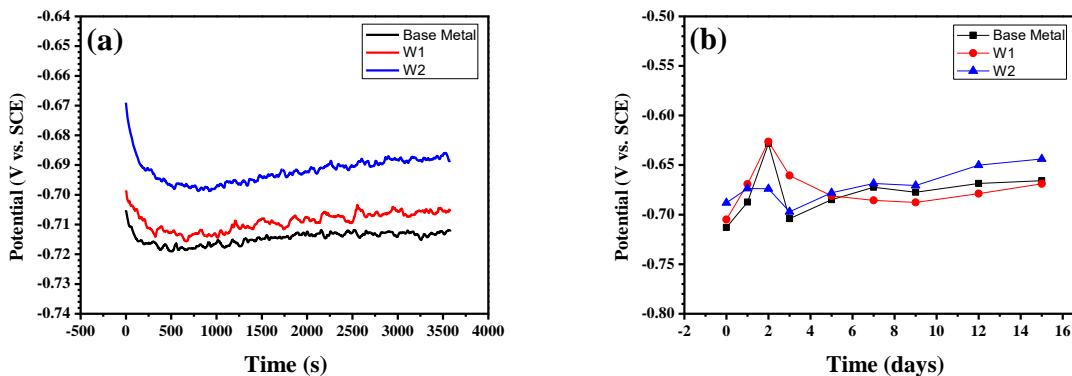
Figure 4. OCP evolution for the base metal, W1 and W2 in the NaHSO$_3$ solution: (a) after 1 h; (b) 1d ~ 16d

3.5 Analysis of potentiodynamic polarization curve

In this section, linear polarization resistance (LPR) and potentiodynamic polarization curves were used to detect the corrosion rate of the specimens. The LPR evolutions for the base metal and specimens W1 and W2 in 0.01 mol/L NaHSO$_3$ solution are shown in Fig. 5. The three specimens present a similar LPR evolution law. The LPR curves increase rapidly in the early stage and reach their maximum values on the second day. Then, they gradually decrease and tend to be stable after the seventh day but increase again at the end of the experiment. In the later period of the experiment, the LPR curves of specimen W2 are higher than those of the base metal and specimen W1, indicating the high corrosion resistance of specimen W2. The LPR results are in accordance with the OCP results.


Figure 5. LPR evolution for the base metal and specimens W1 and W2 in the NaHSO$_3$ solution

The potentiodynamic polarization curves for the base metal, specimens W1 and W2 in 0.01 mol/L NaHSO$_3$ solution for an hour are revealed in Fig. 6, with the fitting results indicated in Table 5. As shown in Fig. 6, the diffusion process dominates the cathodic reactions for the three specimens, while anodic dissolution is responsible for the anodic process. Little difference can be observed between the base metal and specimen W1. However, in comparison with them, specimen W2 displays better corrosion resistance. From the fitting results (Table 5), the most positive free-corrosion potential, the

relatively small corrosion current and the largest Tafel slope are detected for specimen W2. The results indicate that the corrosion rate of specimen W2 is smaller than that for the base metal and specimen W1.
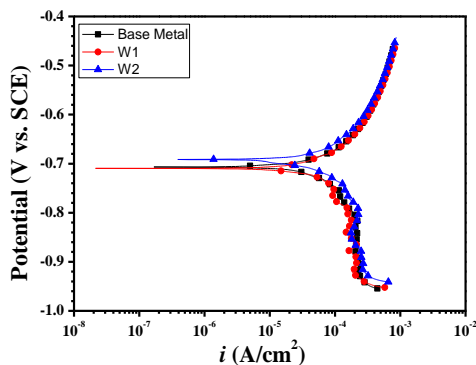

**Figure 6.** Potentiodynamic polarization curves of the base metal, W1 and W2 in the NaHSO₃ solution after 1 h

Table 5. Fitting results of the potentiodynamic polarization curves for the base metal, W1 and W2

Materials	E_{corr} (V vs. SCE)	i_{corr} (A/cm^2)	β_c (mV/dec)	β_a (mV/dec)
Base metal	-0.707	1.72×10^{-4}	448	142
W1	-0.709	1.49×10^{-4}	374	131
W2	-0.692	1.60×10^{-4}	488	145

3.6 EIS analysis

In this section, electrochemical impedance spectroscopy (EIS) is used to study the corrosion process of the specimens. The EIS evolutions for the base metal and specimens W1 and W2 in 0.01 mol/L NaHSO₃ solution are shown in Fig.7. As seen from the figure, the EIS plots for the specimens manifest two capacitance arcs, which are the most common EIS plots for steels in solution [13-14]. The results indicate that the three specimens have similar corrosion processes in the solution. Two time constants can be detected from the EIS plots. The time constant in the high frequency section is relevant to the high frequency phase shift and the corrosion product film, while the time constant in the low frequency section is related to the electric double layer and the charge transfer process on the sample surface [15].
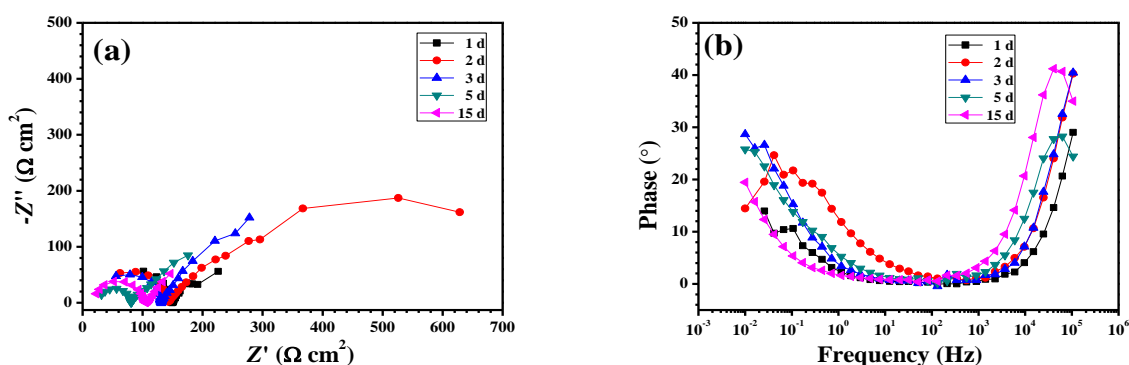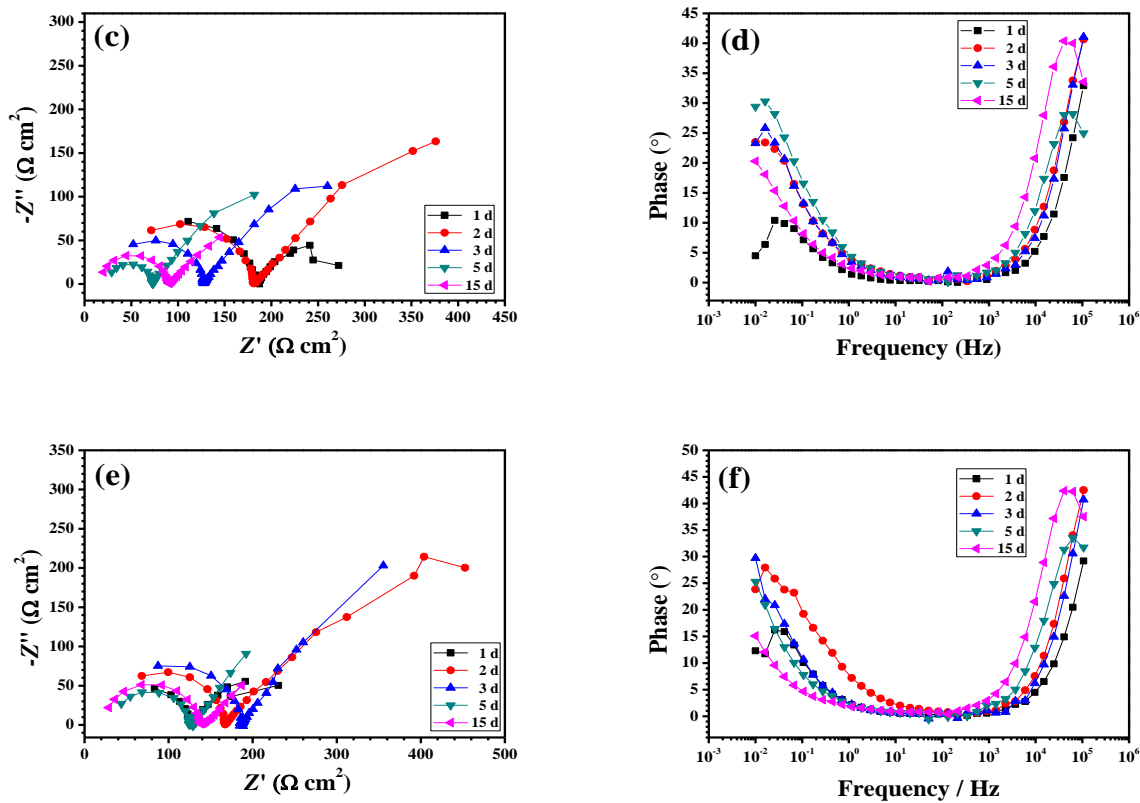
Figure 7. Nyquist and Bode plots in the 0.01 mol/L NaHSO$_3$ solution: base metal (a and b), W1 (c and d) and W2 (e and f)

Based on the above analysis, the EIS plots of the three specimens are fitted via ZsimpWin software by the equivalent circuit model, as shown in Fig. 8. In the equivalent circuit, R_s is the solution resistance, R_f and Q_f are the resistance and capacitance of the corrosion product film, respectively, and R_{ct} and Q_{dl} are the charge transfer resistance and capacitance of the double layer, respectively. The corresponding fitting results for the base metal and specimens W1 and W2 are listed in Tables 6, 7 and 8, respectively.

As shown in the tables, the Q_f values for the base metal and specimen W1 increase during the first two days, decrease after the second day, and then increases again until the end of the experiment. A similar evolution is also found on specimen W2, only without the increase in Q_f on the first day. These evolutions may reflect the generation and transformation of initial oxide films and the formation of corrosion products on the steel surfaces. The charge transfer resistance R_{ct} values for the base metal and specimen W1 also increase during the first two days, decrease after the second day, and then increase again until the end of the experiment. However, R_{ct} for specimen W2 increases over time throughout the experiment. Moreover, R_{ct} for specimen W2 is always higher than those for the base metal and specimen W1, indicating specimen W2 has the lowest corrosion rate in the NaHSO$_3$ solution. The results are consistent with the analysis of the OCP, LPR and potentiodynamic polarization curves.
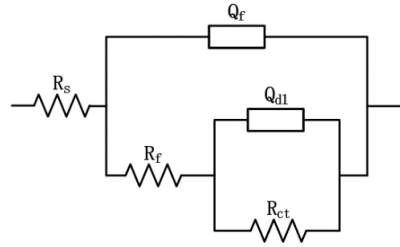
Figure 8. Equivalent circuit model for EIS data fitting

Table 6. EIS fitting results for the base metal

Time d	R_s $\Omega \cdot cm^2$	Q_f $S \cdot sec^n \cdot cm^{-2}$	n_f	R_f $\Omega \cdot cm^2$	Q_{dl} $S \cdot sec^n \cdot cm^{-2}$	n_{dl}	R_{ct} $\Omega \cdot cm^2$
1	49.02	1.496×10^{-8}	0.9526	140.0	0.02697	0.6517	99.01
2	18.33	4.481×10^{-8}	0.9270	124.7	0.00573	0.6205	684.5
3	20.07	4.066×10^{-8}	0.9488	110.6	0.02412	0.6987	583.2
5	25.78	1.962×10^{-7}	0.9442	54.25	0.03173	0.5473	773.7
15	17.39	2.296×10^{-7}	0.9254	86.96	0.07798	0.6002	861.2

Table 7. EIS fitting results for specimen W1

Time d	R_s $\Omega \cdot cm^2$	Q_f $S \cdot sec^n \cdot cm^{-2}$	n_f	R_f $\Omega \cdot cm^2$	Q_{dl} $S \cdot sec^n \cdot cm^{-2}$	n_{dl}	R_{ct} $\Omega \cdot cm^2$
1	7.425	3.527×10^{-8}	0.8787	178.4	0.03624	0.8051	99.35
2	23.73	5.657×10^{-8}	0.9028	158.9	0.01708	0.6306	781.9
3	18.69	4.683×10^{-8}	0.9414	109.1	0.02664	0.6617	509.7
5	23.32	2.230×10^{-7}	0.9393	49.68	0.03632	0.6645	497.3
15	15.96	2.446×10^{-7}	0.9346	73.93	0.05617	0.5496	703.5

Table 8. EIS fitting results for specimen W2

Time d	R_s $\Omega \cdot cm^2$	Q_f $S \cdot sec^n \cdot cm^{-2}$	n_f	R_f $\Omega \cdot cm^2$	Q_{dl} $S \cdot sec^n \cdot cm^{-2}$	n_{dl}	R_{ct} $\Omega \cdot cm^2$
1	12.70	4.381×10^{-8}	0.8884	115.1	0.03596	0.7341	153
2	20.63	3.191×10^{-8}	0.9453	146.5	0.00948	0.6020	937.6
3	21.29	2.200×10^{-8}	0.9501	166.2	0.02749	0.6999	1037
5	30.77	1.355×10^{-7}	0.9209	95.78	0.05045	0.6358	1136
15	21.14	1.773×10^{-7}	0.9217	117.8	0.05912	0.5084	1268

4. DISCUSSION

4.1 Microstructure analysis

Alloy composition is one of the important factors in the microstructure evolution of the weld metal [16]. As shown in Table 1, compared with specimen W1, more Ni but less C and S exist in

specimen W2. In addition, more micro-alloy elements Ti, Mo and V are added in specimen W2. As is reported [16], the increase in alloying additions will raise the hardenability for alloys and shift the weld metal continuous cooling transformation (WM-CCT) curves towards longer times and lower temperatures. Therefore, the transformation product can change from proeutectoid ferrite and ferrite side plate to predominately acicular ferrite and bainite. Element Ni can improve austenite stability and lower microstructure transformation temperature, thus promoting acicular ferrite formation[17]. Element Ti can combine with O and other elements to form sufficient inclusions; the inclusions are dispersed in the weld metal and act as the nucleation sites for acicular ferrite [18]. Therefore, many acicular ferrites have been observed in specimen W2, as shown in Fig. 1c. Elements Mo and V further refine the grain size of the weld metal through precipitation hardening; thus, finer grains exist in specimen W2 in comparison with the base metal and specimen W1 (Fig. 1).

The oxygen content is another major factor in the microstructure evolution of the weld metal [19]. Shielding gas and slag will be generated during the welding chemical metallurgy reaction of flux-cored wire arc welding to protect the weld pool from air invasion. Under the combined protection of 100% CO_2 and the shielding gas generated by the flux-cored wire, the oxygen content in the weld metal can be more effectively reduced in comparison with solid wire arc welding. A low oxygen content can enhance the formation of effective inclusions which can act as favorable nucleation sites for acicular ferrite. Therefore, fine acicular ferrite can be generated in specimen W2 via flux-cored wire (Fig. 1c).

4.2 Corrosion resistance analysis

As presented by Cao et al., the polarization impedance (R_p, Ω cm^2) of the steel can be expressed by the following [20]:

$$R_p = (Z_F)_{\omega=0} \qquad (1)$$

Where, Z_F and ω are the impedance of the steel and the frequency of the sinusoidal signal, respectively. In this paper, the equivalent circuit model of Fig. 10 is used to simulate the EIS data, and equation (1) can be rewritten as follows:

$$R_p = (Z_F)_{\omega=0} \approx R_f + R_{ct} \qquad (2)$$

Then, the corrosion current density (mA/cm^2) is obtained as follows [21]:

$$i_{corr} = B / R_p \qquad (3)$$

where B (mV) is a Stern-Greary constant of 26 mV in this experiment. In this way, the corrosion current density of steel can be simply extracted from EIS data, which is a method that has been widely used in references [21-23].
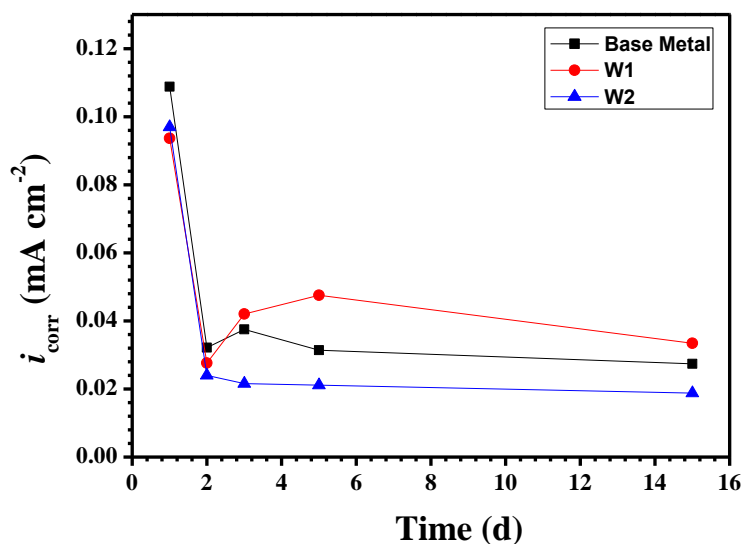
Figure 9. Corrosion current density derived from the EIS of the base metal and specimens W1 and W2 in the 0.01 mol/L NaHSO$_3$ solution as a function of time

The corrosion current densities (i_{corr}) of the three specimens are shown in Fig. 9. For the i_{corr} values of the base metal and specimen W1, they decrease during the first two days, increase after the second day, and then decrease again until the end of the experiment. However, i_{corr} for specimen W2 decreases over time throughout the experiment. Moreover, i_{corr} for specimen W2 is always smaller than those for the base metal and specimen W1, indicating it has the lowest corrosion rate in the NaHSO$_3$ solution.

Based on the above results, three factors may be responsible for the above change in the corrosion current density of the three specimens. The first is the evolution of the initial film and the corrosion product layer[3,6]. When the specimens were exposed to the NaHSO$_3$ solution, an oxide film may be generated on the surface with the help of oxygen and keep the corrosive ions from the metal/solution interface, which may lead to the decrease in corrosion current density. This is the reason for the decrease in corrosion current density during the first two days. Then, under the action of the corrosive ions in solution, the oxide film may be gradually permeated, resulting in the increase in the corrosion current density for the base metal and specimen W1. After that, the corrosion product may deposit on the surface and play a role in hindering the corrosion process, which is the reason for the decrease in corrosion current density at the end of the experiment. For specimen W2, because the composition and construction of the corrosion product are different from those of the base metal and specimen W1, the more remarkable inhibiting effect counteracts the increase in corrosion current density. Therefore, i_{corr} for specimen W2 decreases over time throughout the experiment.

The second is the cracks generated on the corrosion product. Although the corrosion products on the base metal and specimen W1 are compact and integrated, some small cracks are detected on the surface and inside the corrosion products. However, no cracks are observed on the corrosion products of specimen W2, reflecting the good mechanical properties of this corrosion product. The cracks may

provide channels for the corrosive ions to diffuse through the corrosion product, which would enhance the corrosion process [24].

The third is the alloying elements. Alloying elements play an important role in the resistance of weathering steel to atmospheric corrosion. When the Ni content reaches 0.11% or more, the corrosion resistance of steel will gradually improve with more Ni content [25]. Element Ni is favorable for improving the α-FeOOH content in the rust layer and increases the density and resistance of the rust layer[26]. Element Cr can diffuse into the Fe lattice and replace some Fe atoms, thus forming multiple-component oxides. Multiple-component oxides easily precipitate where cracks and holes form, thus accelerating defect healing [27,28] and inhibiting the entry of corrosive ions. The contents of the alloying elements in specimen W2 are higher than those in the base metal and specimen W1 (Table 1). In addition, the alloying elements are also rich in the inner corrosion product film (Fig. 3 and Table 4). Therefore, the corrosion rate of specimen W2 is limited.

5. CONCLUSIONS

1. Ferrite and pearlite are the main microstructures of the base metal. The microstructure of specimen W1 is mainly consisted of proeutectoid ferrite and side plate ferrite. Fine acicular ferrite and granular bainite are crossly distributed in specimen W2, with some side plate ferrite and polygonal ferrite.

2. Compact and integrated corrosion products cover the surface of the three specimens, however, there are some small cracks on the surface of the base metal and specimen W1. In contrast, there are no cracks observed in corrosion product morphologies of specimen W2.

3. In the later period of the experiment, the LPR curves of specimen W2 are higher than those of the base metal and specimen W1. The most positive free-corrosion potential, a relatively small corrosion current and the largest Tafel slope reflect that specimen W2 has the smallest corrosion rate.

4. The three specimens have similar corrosion processes in the solution. The composition, generation and evolution of the corrosion product layer play an important role in the corrosion process.

5. The flux-cored wire is a potential and viable weld wire choice for gas metal arc welding.

References

1. C. N. Cao, The natural environment corrosion of materials in China, Chemical Industry Press, (2005)Beijing, China
2. M. Morcillo, I. Díaz, B. Chico, H. Cano, D. De La Fuente, *Corros.Sci.*, 83(2014)6.
3. T. Kamimura, S. Hara, H. Miyuki, M. Yamashita, H. Uchida, *Corros.Sci.*, 48(2006)2799.
4. M. Yamashita, H.Miyuki, Y.Matsuda, H.Nagno, T.Misawa, *Corros.Sci.*, 36(1994)28.
5. S. T. Wang, S. W. Yang, K. W. Gao, X. L. He, *Int.J.Min.Met.Mater.*, 16(2009)58.

6. H. Y. Wu, H.G.Lei,Y.F.Chen,J.Y.Qiao,*Constr.Build.Mater.*, 211(2019)228.
7. M. Morcillo, I. Díaz, H. Cano, B. Chico, D. De La Fuente,*Constr.Build.Mater.*, 213(2019)723.
8. X. F. Yin, H. J. Xu, W. W. Zhao, *Journal of Dalian Jiaotong University*, 30(2009) 45.
9. M. T. Liao, W. J. Chen, *Int. J. Adv. Manuf. Tech.*, 15(1999)49.
10. F. C. Yin, M. H. Zhang, B. Hong, A kind of flux-cored wire with high toughness and corrosion resistance to atmospheric environment and its preparation technology, *China Paten*, ZL201610224365.1
11. B. Hong, M. H. Zhang, F. C. Yin, *Transactions of the China Welding Institution*, 38(2017) 67.
12. Y. T. Ma, Y. Li, F. H. Wang, *Corros.Sci.*, 51(2009)997.
13. A. Nishikata, Q. J. Zhu, E. Tada, *Corros.Sci.*, 87(2014)80.
14. S. X. Wang, D. X. Liu, N. Du, Q. Zhao, J. H. Xiao, *Int. J. Electrochem. Sci.*,11(2016)2534.
15. T. Wu, J. Xu, C. Sun, M. Yan, C. Yu,W. Ke, *Corros.Sci.*, 88(2014)291.
16. K. Sindo, Welding Metallurgy, 2nd Ed., John Wiley & Sons, Inc., (2002) New Jersey, America
17. S. D. Bhole, J. B. Nemade, B. L. Collins, *C. Liu. J. Mater. Process Tech,* 173(2006)92.
18. B. Beidokhti, H. Koukabia, A. Dolati, *J. Mater. Process Tech.,* 209(2009)4027.
19. M. I. Onsoien, S. Liu, D. L. Olson, *Weld. J.*, 75(1996) 216.
20. C. N. Cao, Principles of Electrochemistry of Corrosion, 3rd Ed., Chemical Industry Press, (2008)Beijing, China
21. L. Hao, S. Zhang, J. Dong, W. Ke, *Corros. Sci.*, 58 (2012) 175.
22. R.P.V. Cruz, A. Nishikata, T. Tsuru, *Corros. Sci.*, 38 (1996) 1397.
23. T. Nishimura, *Corros. Sci.*, 52 (2010) 3609.
24. S. J. Travassos, C. R. Tomachuk, H. G. de Melo, *Electrochimi. Acta*, 325(2019)1.
25. Z. Y. Liu, X. L. He, J. Q. Chen, *S. W. Yang*, *B. W. Chen*, *M.Hu*, *W. Liang* , *Advanced Materials Research*, 295(2011)1436.
26. X. Z. Zhang, L. J. Gao, Z. C. Yao, X. Zhang, *Transactions of the China Welding Institution*, 40(2019) 154.
27. C. Lin, X. G. Li, X. D. Liu, *J. Chin. Soc. Corro. Prot.*, 25(2005)193.
28. I. Díaz, H. Cano, P. Lopesino, D. De La Fuente, B. Chico, *Corros.Sci.*, 141(2018)146.